EASR

Engineering and Applied Science Research

https://www.tci-thaijo.org/index.php/easr/index

Published by the Faculty of Engineering, Khon Kaen University, Thailand

Comparative analysis of steady and unsteady friction models in numerical simulation of water hammer phenomenon

Zakariya Mohsin*[1)], Zeyad Sulaiman[2)] and Sahad Khilqa[3)]

[1)]Presidency of University, University of Telafer, Tal Afar, Iraq
[2)]Department of Dams and Water Resources, Collage of Engineering, University of Mosul, Mosul, Iraq
[3)]Richland County Utilities, South Carolina, USA

Received 22 November 2024
Revised 11 February 2025
Accepted 18 February 2025

Abstract

This study presents comparative numerical modeling using the method of characteristics to solve the water hammer phenomenon in a pipeline that consists of reservoir-pipe-valve systems resulting from an instantaneous valve closure. Study focused on the unsteady friction approach, the two-coefficient instantaneous acceleration-based unsteady friction model (2-k IAB), which describes the transient flow behavior in pipeline systems during rapid velocity changes that result in water hammer events. Also, the methodology includes developing a mathematical model based on the numerical simulation of the governing equations using the proposed models and validating the model results by utilizing six sets of experimental data from two different laboratory sources. The study compares the performance of steady and unsteady friction models and reveals the limitations and advantages of each in simulating pressure waves resulting from the water hammer. The study also discusses the basic criteria for selecting k_{ut} values when using the average wave speed for experimental data. Numerical results show that the best model and the most consistent with experimental data is the 2-k IAB model, followed by the one-coefficient instantaneous acceleration-based model (1-k IAB), and finally, the least accurate model is the steady friction model. This was validated by using the statistical method Normalized Root Mean Squared Error. The methodology presented in this paper can be a valuable tool for analyzing and designing pipeline systems subjected to the water hammer phenomenon. It provides insights into transient flow characteristics resulting from instantaneous valve closure and helps determine the appropriate mitigation measures to prevent pipeline system damage.

Keywords: Water hammer, Transient flow, Unsteady friction models, Method of characteristics, Two-coefficient instantaneous acceleration-based

1. Introduction

One of the common, risky issues facing water transport pipelines is the water hammer phenomenon, which occurs when there is a rapid change in flow velocity. This occurrence is attributed to various factors, including but not limited to the start-up or shutdown of pumps, opening or closing of valves [1]; that may cause a significant change in pressure. The change in pressure propagates in waves across the system at very high speeds. The pressure waves oscillate until they dissipate due to energy loss [2]. Water hammer can lead to catastrophic damage if not understood and managed properly. Therefore, it is essential to analyze the impact of water hammers on pipelines, which are pillars of successful and economical system design. Appropriate protection systems and safe operational guidelines are recommended to avoid and protect the system from damage [3]. Historically, researchers faced significant challenges in analyzing water hammer due to the nonlinear nature of the governing equations of transient flows. From few attempts to find analytical solutions by driving a close-form of these equations, Urbanowicz et al. [4] and Urbanowicz et al. [5] have proposed analytical solutions for simple configuration of water hammer setup. Joukowsky presented a simplified analytical solution by applying Newton's second law under certain conditions and assumptions [6]. However, this solution was inherently limited and could only estimate the peak of the first pressure wave in a water hammer event. The significant advancements in computer technology and its commercial availability marked a turning point in simulating water hammer. Thanks to the computational power these devices offer, researchers could use numerical methods to analyze water hammer events in more complex systems with more detail by executing thousands of computations in short time periods [7]. Choosing the right numerical method and friction models is crucial to predicting transient behavior in pipe systems during water hammer modeling [8]. One such numerical method that has shown significant potential and is extensively used in the analysis of water hammer is the Method of Characteristics (MOC). This method transforms partial differential equations into a set of ordinary differential equations that can be solved along specific paths called characteristics [9].

Numerous research studies have compared various numerical methods and friction models for water hammer simulations. Bhattacharyya et al. [10] studied the water hammer simulation using the MOC to solve the partial differential equations, employing steady friction models by finding the Darcy friction factor in two ways. They obtained the same first (maximum) pressure wave, and discharge curves were calculated using both methods. On the other hand, Yu et al. [11] addressed the limitations associated with the

*Corresponding author.
Email address: zakariya.z.mohsin@uotelafer.edu.iq
doi: 10.14456/easr.2025.18

quasi-steady friction model. They proposed a new method for handling the friction term based on the Moody diagram using the MOC. The results show that the simulation of pressure wave damping aligns well with the experimental data used. It was observed in this experiment that absolute roughness had a minor effect on the result, while the minimum Reynolds number had a more significant impact. This finding aligns with [12], who also reported a more pronounced effect of the minimum Reynolds number. While Abdeldayem et al (8) conducted a comparison of friction models using commercial software. They concluded that the unsteady friction model is the most effective and suitable for water hammer simulations, as it excellently captures the water hammer wave. Similarly, Kjerrumgaard Jensen et al. [13] findings revealed that unsteady friction models, including the Instantaneous-Acceleration-Based (IAB) and Convolution Integral models, were more effective in capturing the pressure wave than the quasi-steady model using the Method of Characteristics. On the other hand, Prashanth Reddy et al. [14] conducted a comparative study of 2-k IAB unsteady friction models: 1-k IAB and 2-k IAB. Furthermore, they conducted a comprehensive study on damping coefficients. Based on the results, the 2-k IAB models demonstrated a better fit to the experimental data than the 1-k IAB models. In addition, they found that the values of damping coefficients decrease as the Reynolds number increases. While Convolution Integral models, which account for the full history of transient flow through weighting functions, have demonstrated high theoretical accuracy in capturing unsteady friction effects, their computational complexity has limited widespread adoption in practical engineering simulations [15]. Recent advancements, however, have simplified these models using effective weighting functions composed of two exponential terms, significantly reducing computational costs while maintaining sufficient accuracy in simulating pressure wave damping [16].

Friction models are important in simulating the propagation of pressure waves and the dissipation of energy within pipe systems. The steady friction model accounts solely for losses due to wall friction, whereas the unsteady friction model considers dynamic changes in fluid flow characteristics during transient occurrences [17]. The present study focuses on analyzing IAB models, as its primary objective is to evaluate the performance of less theoretically complex models under diverse flow conditions. This research addresses a critical limitation of the 1-k IAB model – the inability to accurately simulate the propagation of water hammer waves. To overcome this limitation, the study focuses on developing and evaluating a 2-k IAB unsteady friction model. The goal is to examine the model's performance compared to the 1-k IAB unsteady friction and steady friction models. This study not only delineates the strengths and weaknesses of each model but also validates them against a diverse range of experimental data derived from relevant literature. The core significance of the work is embodied in the capacity to augment the precision of water hammer modeling, leading to a substantial way to implement safer and more efficient water transport systems.

2. Research methodology

The paper begins by explaining the construction of the numerical model, with a special focus on deriving the governing equations using the 2-k IAB unsteady friction model and the MOC. Following this, the paper presents the simulation results and performs a comparative performance analysis. This comparison focuses on the developed 2-k IAB unsteady friction model, the 1-k IAB unsteady friction model, and the steady friction model, examining their capabilities in simulating water hammer waves. Additionally, a trial-and-error technique will be used to estimate the damping coefficients of these models. To compare the accuracy of the different friction models, the statistical method Normalized Root Mean Squared Error (NRMSE) was used as a statistical analysis tool for this study [14]. The NRMSE is a standard metric used in data analysis to estimate the average size of the error between a set of calculated values and the actual observed values. The calculation of NRMSE requires determining the square root of the mean squared variances (RMSE) divided by the range of observed values, as described in $\text{NRMSE} = \sqrt{\sum_{i=1}^{n} \frac{(P_i - O_i)^2}{n}} / (O_{max} - O_{min})$. Where P_i and O_i are the calculated and observed values, n is the total number of observed values, and O_{max} and O_{min} are the maximum and minimum values of the observed values, respectively.

3. Numerical model development

The development of a numerical model for water hammer analysis represents the construction of a computational schema designed to simulate and investigate transient phenomena within piping systems. Key steps in this process include the selection of a suitable numerical approach, the integration of friction models, the establishment of governing equations, considerations for boundary conditions, and the obtaining experimental data [18]. Crafting a precise and efficient numerical model is of paramount importance in comprehending and alleviating the effects of water hammer events on pipeline systems [19]. This research endeavors to explore the numerical representation of transient flows. Specifically, the simulation focuses on a system consisting of a reservoir, pipe, and valve at the pipe's end. The investigation utilizes three distinct friction models: steady and two unsteady friction models, which are applied through the MOC. The primary objective is to provide a deeper understanding of the impact of selecting the appropriate friction model on the accuracy of the simulation results.

3.1 Numerical method

This study uses the MOC to solve the governing equations of transient pipe flows. The fundamental principle behind the Method of Characteristics involves converting partial differential equations (PDEs)—which include time as an independent variable and describe the conservation of mass and momentum for a fluid flowing through a pressurized pipe over time to ordinary differential equations (ODEs). These ODEs can be resolved along distinct paths, termed 'characteristics' [9] within the space-time domain that describe the system's flow behavior along the pipe [20]

3.2 Friction models

This research incorporates three distinct types of friction models: a steady friction model and two coefficients unsteady friction models. The steady friction model used in this study is based on the Darcy-Weisbach equation. It represents the pressure change loss resulting from the friction against the pipe wall of the flow [9], which is characterized as follows:

$$J_s = \frac{f}{D}\frac{v^2}{2g} \tag{1}$$

where J_s represents the steady friction head loss per unit length, while f is Darcy-Weisbach friction factor, D is the diameter of the pipe, v denotesthe flow velocity, and g is the gravitational acceleration. Regarding the unsteady friction models, two such models were considered: the 1-k IAB model, which considers additional friction losses such as the flow changes in acceleration and its resistance to this change that occur during transient flow conditions where flow and pressure change rapidly in addition to the friction of the flow against the pipe wall. This model combines the effects of local acceleration and convective acceleration together using a single damping coefficient [12].

$$J_u = \frac{k}{g}\left(\frac{\partial v}{\partial t} + \emptyset\, a\frac{\partial v}{\partial x}\right) \tag{2}$$

where J_u is the head loss per unit length due to unsteady friction, while k is the damping coefficient associated with instantaneous acceleration. Additionally, a symbolizes the wave speed within the pipe. Moreover, t and x represent time and distance, respectively. $\emptyset$ represents the sign of the term for convective acceleration, which aids in capturing the additional damping effects arising from convective acceleration. It does so by considering the direction of the velocity gradient and its impact on the total energy damping within the system [21].

$$\emptyset = sign\left(v\,\frac{\partial v}{\partial x}\right) \tag{3}$$

The second unsteady friction model is the 2-k IAB model. This model distinguishes itself from the one-coefficient model by separating the effects of local acceleration from convective acceleration and utilizing two different coefficients for each type of acceleration [22].

$$J_u = \frac{1}{g}\left[k_{ut}\frac{\partial v}{\partial t} + k_{ux}\emptyset\, a\frac{\partial v}{\partial x}\right] \tag{4}$$

where k_{ut} is the local acceleration coefficient, which has been numerically proven to influence the speed of pressure waves that slightly affects the damping rate [23], while k_{ux} is the convective acceleration coefficient, which has been numerically demonstrated to affect the damping rate. Despite the various methods to determine damping coefficients, selecting the appropriate coefficient for certain cases remains challenging when applying the IAB model. In this study, the researchers use a trial-and-error method to ascertain the damping coefficient k's value. In addition, with regard to the local acceleration coefficient k_{ut} and the convective acceleration coefficient k_{ux} , the convective acceleration coefficient k_{ux} is the same as the damping coefficient k. When the value of k_{ut} is set to zero, it is fused to correct the wave speed in the simulation [15]. This means using the correct wave speed for the experiment as an average wave speed may lead to better results when replacing the value of k_{ut} with zero. In analyzing water hammer phenomena, integrating an unsteady friction term is paramount to precisely capture the transient flow behavior of the piping system, especially during abrupt alterations in flow rate or pressure. Incorporating this term within the governing equations enables the numerical model to yield more trustworthy and accurate outcomes, thereby improving our understanding and management of water hammer events [23]. In addition, the choice of the appropriate unsteady friction model is also a crucial factor. Selecting a suitable model contributes to a more precise simulation, resulting in a better prediction of system behavior and, subsequently, more effective mitigation strategies.

3.3 Governing equations

To derive the governing equation for the characteristic's method with the 2-k IAB Unsteady Friction Model, we consider the one-dimensional partial differential equations for unsteady flow in a pipe and determine the linear combination of these equations.

$$Mass\ Continuity\ equation: \quad \frac{\partial H}{\partial t} + \frac{a^2}{g}\frac{\partial v}{\partial x} = 0 = L_1 \tag{5}$$

$$Momentum\ equation: \quad \frac{\partial H}{\partial x} + \frac{1}{g}\frac{\partial v}{\partial t} + J_u + J_s = 0 = L_2 \tag{6}$$

H represents the piezometric head, v signifies the flow velocity, a denotes the wave speed, and g is the gravitational acceleration. The variable t stands for time, x is the distance, and both J_u and J_s are terms for friction losses. The Equations Linear Combination:

$$L_2 + \lambda\, L_1 = 0 \tag{7}$$

where λ is an unknown multiplier [9]. By using Eq.5 & Eq.6 at Eq.7, we get:

$$\lambda\left(\frac{\partial H}{\partial t} + \frac{1}{\lambda}\frac{\partial H}{\partial x}\right) + \frac{1+k_{ut}}{g}\left(\frac{\partial v}{\partial t} + \frac{\emptyset k_{ux} a + \lambda\, a^2}{1+k_{ut}}\frac{\partial v}{\partial x}\right) + \frac{f}{D} * \frac{v^2}{2g} = 0 \tag{8}$$

To convert the Partial Differential Equations (PDEs) into Ordinary Differential Equations (ODEs), using the total derivative as:

$$\frac{d\beta}{dt} = \frac{\partial \beta}{\partial t} + \frac{dx}{dt}\frac{\partial \beta}{\partial x} \tag{9}$$

Here, β is the characteristics of fluid (H, v). By using this mathematical concept in Eq.8, we get:

$$\frac{gA\lambda}{1+k_{ut}}\frac{dH}{dt}+\frac{dQ}{dt}+\frac{f\,Q|Q|}{2DA(1+k_{ut})}=0 \quad , \qquad Assume \quad R=\frac{f}{2DA}$$

$$\frac{gA\lambda}{1+k_{ut}}\frac{dH}{dt}+\frac{dQ}{dt}+\frac{R}{1+k_{ut}}Q|Q|=0 \tag{10}$$

The constraint that results from transforming PDEs into ODEs is the limited operation of the ODEs within the characteristic lines only. Therefore, through the following, we will find the slope of the characteristic lines:

$$\frac{1}{\lambda}=\frac{dx}{dt}=\frac{\emptyset k_{ux}a+\lambda\, a^2}{1+k_{ut}}$$

$$\frac{1}{\lambda}=\frac{\emptyset k_{ux}a+\lambda\, a^2}{1+k_{ut}}\rightarrow a^2\lambda^2+\emptyset k_{ux}a\lambda-(1+k_{ut})=0\rightarrow$$

$$\lambda_{(+)}=\frac{-\emptyset k_{ux}+(2+k_{ut})}{2a}, \qquad \lambda_{(-)}=\frac{-\emptyset k_{ux}-(2+k_{ut})}{2a}$$

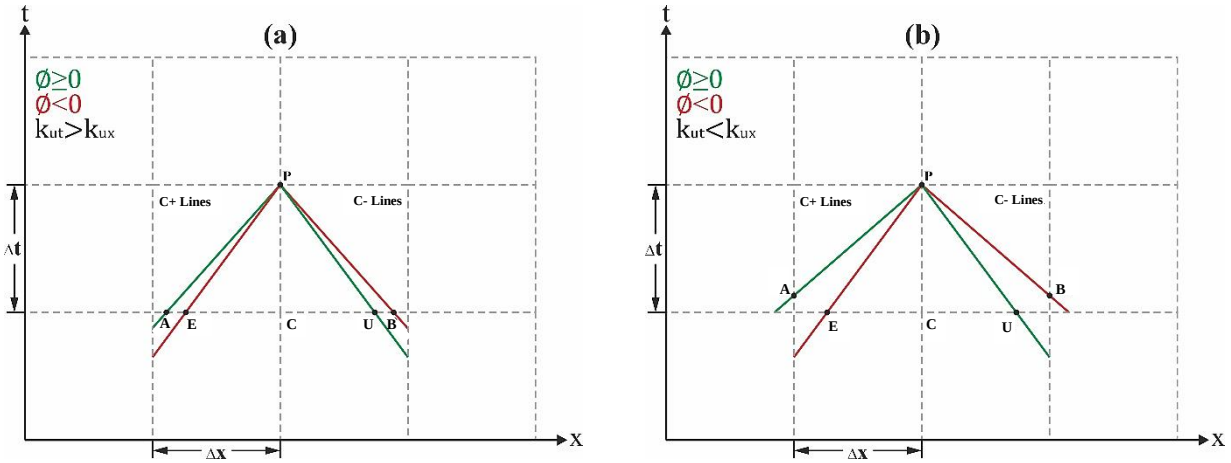

Figure 1 Characteristic lines in the x-t plan: (a) when $k_{ut} > k_{ux}$, (b) when $k_{ut} < k_{ux}$.

The choice of the Courant number Cn, which is the ratio of the wave speed of the fluid to the numerical wave speed (Δx/Δt), is an essential part of MOC [9]. This dimensionless parameter impacts the stability and accuracy of the numerical outcome, and it is generally recommended that it be equal to or less than 1 [24] Based on the concept of the Courant number, we will utilize wave speed as the slope for the Characteristic Grid. In our study, the Courant number is assumed to be equal to 1, which is a common value in water hammer analysis. This balances numerical stability, accuracy, and computational efficiency.

$$C_n=\frac{a}{\Delta x/\Delta t}\leq 1$$

where C_n represents the Courant number, a denotes the wave speed, Δx is indicative of the spatial step size, and Δt is the time step size. Depending on the sign of $\emptyset$ and which of the damping coefficients is larger between k_{ux} and k_{ut}, as shown in the Figure 1, the slope of the characteristic lines will be as shown in the Table 1.

Table 1 Possible cases for the slope of characteristic lines

$\emptyset$	$\boldsymbol{\lambda}$ **Sign**	**slope** $=\boldsymbol{\lambda}$		**The line intersects with**
+1	+	$\lambda_{(+)}=-k_{ux}+(2+k_{ut})/2a$	$k_{ut}>k_{ux}$	Space Domain
+1	−	$\lambda_{(-)}=-k_{ux}-(2+k_{ut})/2a$		Space Domain
−1	+	$\lambda_{(+)}=k_{ux}+(2+k_{ut})/2a$		Space Domain
−1	−	$\lambda_{(-)}=k_{ux}-(2+k_{ut})/2a$		Space Domain
+1	+	$\lambda_{(+)}=-k_{ux}+(2+k_{ut})/2a$	$k_{ut}<k_{ux}$	Time Domain
+1	−	$\lambda_{(-)}=-k_{ux}-(2+k_{ut})/2a$		Space Domain
−1	+	$\lambda_{(+)}=k_{ux}+(2+k_{ut})/2a$		Space Domain
−1	−	$\lambda_{(-)}=k_{ux}-(2+k_{ut})/2a$		Time Domain

Identifying characteristic line slopes allows us to define two distinct sets of lines, labeled as C_+ and C_-; along these lines, the ordinary differential equations (ODEs) can be resolved, as depicted in Figure 1. The derivation of characteristic lines, C_+ and C_-, is accomplished by employing the slope values found in Table 1, by the following steps:

1. When $k_{ut} > k_{ux}$, $\emptyset \geq 0$, $\frac{dx}{dt} = \frac{1}{\lambda_{(+)}} = \frac{2a}{-k_{ux}+(2+k_{ut})}$

By substituting $\lambda_{(+)}$ in Eq.10 we get:

$$\frac{gA}{1+k_{ut}} * \frac{-k_{ux}+(2+k_{ut})}{2a} dH + dQ + \frac{R}{1+k_{ut}} Q|Q|\, dt = 0$$

Assuming that $c_a = \frac{gA}{a}$, $T_{np} = \frac{(-k_{ux}+(2+k_{ut}))}{2(1+k_{ut})}$

$$c_a T_{np} \int_A^P dH + \int_A^P dQ + \frac{R}{1+k_{ut}} \int_A^P Q|Q|\, dt = 0 \rightarrow$$

Here, we'll assume that the equation's final term remains constant over time, as there's no explicit solution for this term outside of approximation methods. Proceeding with the integration of the equation, we obtain:

$$c_a T_{np}(H_P - H_A) + Q_P - Q_A + \frac{R}{1+k_{ut}} Q_A|Q_A|\, \Delta t = 0 \rightarrow$$

Employing this, we may formulate the equation for the positive characteristic line, C_+. This equation is crucial for calculating the discharge at node P at the subsequent time interval, $t + \Delta t$, as depicted below:

$$C_+ = Q_A + c_a T_{np} H_A - \frac{R}{1+k_{ut}} Q_A|Q_A|\, \Delta t \tag{11}$$

$$Q_P = C_+ - c_a T_{np} H_P \tag{12}$$

Given that the properties of the fluid are only recognized at the nodes within the characteristic grid in the space-time domain, it becomes necessary to utilize interpolation methods. These techniques are used to identify the characteristics at points of intersection between the characteristic lines and the grid. Since the characteristic line intersects with the distance axis, the interpolation in this case is called Space Domain Interpolation and it's as follows:

$$\beta_A = \beta_C - \frac{2(\beta_C - \beta_N)}{-k_{ux}+(2+k_{ut})} \tag{13}$$

Where, β is a property of fluid (Q, H).

2. When $k_{ut} > k_{ux}$, $\emptyset \geq 0$, $\frac{dx}{dt} = \frac{1}{\lambda_{(-)}} = \frac{2a}{-k_{ux}-(2+k_{ut})}$

Utilizing the same steps, we can formulate the equation for the negative characteristic line C_-. This will enable us to determine the discharge at the P node at the time interval $t + \Delta t$.

$$C_- = Q_U + c_a T_{nn} H_U - \frac{R}{1+k_{ut}} Q_U|Q_U|\, \Delta t \tag{14}$$

$$Q_P = C_- - c_a T_{nn} H_P \tag{15}$$

$$\beta_U = \beta_C - \frac{2(\beta_F - \beta_C)}{-k_{ux}-(2+k_{ut})} \tag{16}$$

$$Where, \quad T_{nn} = \frac{(-k_{ux}-(2+k_{ut}))}{2(1+k_{ut})}$$

3. When $k_{ut} > k_{ux}$, $\emptyset < 0$, $\frac{dx}{dt} = \frac{1}{\lambda_{(+)}} = \frac{2a}{k_{ux}+(2+k_{ut})}$

Following similar steps, we may determine the equation for the positive characteristic line C_+. This will aid in determining the discharge at the P node for the time interval $t + \Delta t$.

$$C_+ = Q_E + c_a T_{pp} H_E - \frac{R}{1+k_{ut}} Q_E|Q_E|\, \Delta t \tag{17}$$

$$Q_P = C_+ - c_a T_{pp} H_P \tag{18}$$

$$\beta_E = \beta_C - \frac{2(\beta_C - \beta_N)}{k_{ux}+(2+k_{ut})} \tag{19}$$

$$Where, \quad T_{pp} = \frac{(k_{ux} + (2 + k_{ut}))}{2(1 + k_{ut})}$$

4. When $k_{ut} > k_{ux}$, $\emptyset < 0$, $\frac{dx}{dt} = \frac{1}{\lambda_{(-)}} = \frac{2a}{k_{ux} - (2 + k_{ut})}$

Similarly, to calculate the discharge at the P node for the time interval $t + \Delta t$ in this case, we will use following negative characteristic line equation C_-:

$$C_- = Q_B + c_a T_{pn} H_B - \frac{R}{1 + k_{ut}} Q_B |Q_B| \, \Delta t \tag{20}$$

$$Q_P = C_- - c_a T_{pn} H_P \tag{21}$$

$$\beta_B = \beta_C - \frac{2(\beta_F - \beta_C)}{k_{ux} - (2 + k_{ut})} \tag{22}$$

$$Where, \quad T_{pn} = \frac{(k_{ux} - (2 + k_{ut}))}{2(1 + k_{ut})}$$

5. When $k_{ut} < k_{ux}$, $\emptyset < 0$, $\frac{dx}{dt} = \frac{1}{\lambda_{(+)}} = \frac{2a}{-k_{ux} + (2 + k_{ut})}$

The C_+ equation derivation in this case is the same as the derivation of the equation from the first case, which is:

$$C_+ = Q_A + c_a T_{np} H_A - \frac{R}{1 + k_{ut}} Q_A |Q_A| \, \Delta t \tag{23}$$

$$Q_P = C_+ - c_a T_{np} H_P \tag{24}$$

Since the characteristic line intersects with the time axis, the interpolation in this case is called Time Domain Interpolation and it's as follows:

By assuming $\beta_G - \beta_A \approx \beta_C - \beta_N \rightarrow \beta_G = \beta_C + \beta_J - \beta_N$

$$\beta_A = \frac{\beta_C - \beta_N}{a} + \beta_N - \frac{\beta_C - \beta_N}{2a}\left(-k_{ux} + (2 + k_{ut})\right) \tag{25}$$

6. When $k_{ut} < k_{ux}$, $\emptyset \geq 0$, $\frac{dx}{dt} = \frac{1}{\lambda_{(-)}} = \frac{2a}{-k_{ux} - (2 + k_{ut})}$

The C_- equation derivation in this case is the same as the derivation of the equation from the second case, which is:

$$C_- = Q_U + c_a T_{nn} H_U - \frac{R}{1 + k_{ut}} Q_U |Q_U| \, \Delta t \tag{26}$$

$$Q_P = C_- - c_a T_{nn} H_P \tag{27}$$

$$\beta_U = \beta_C - \frac{2(\beta_F - \beta_C)}{-k_{ux} - (2 + k_{ut})} \tag{28}$$

7. When $k_{ut} < k_{ux}$, $\emptyset < 0$, $\frac{dx}{dt} = \frac{1}{\lambda_{(+)}} = \frac{2a}{k_{ux} + (2 + k_{ut})}$

The C_+ equation derivation in this case is the same as the derivation of the equation from the third case, which is:

$$C_+ = Q_E + c_a T_{pp} H_E - \frac{R}{1 + k_{ut}} Q_E |Q_E| \, \Delta t \tag{29}$$

$$Q_P = C_+ - c_a T_{pp} H_P \tag{30}$$

$$\beta_E = \beta_C - \frac{2(\beta_C - \beta_N)}{k_{ux} + (2 + k_{ut})} \tag{31}$$

8. When $k_{ut} < k_{ux}$, $\emptyset < 0$, $\frac{dx}{dt} = \frac{1}{\lambda_{(-)}} = \frac{2a}{k_{ux} - (2 + k_{ut})}$

The C_- equation derivation in this case is the same as the derivation of the equation from the fourth case, which is:

$$C_{-} = Q_B + c_a T_{pn} H_B - \frac{R}{1 + k_{ut}} Q_B |Q_B| \, \Delta t \tag{32}$$

$$Q_P = C_{-} - c_a T_{pn} H_P \tag{33}$$

$$\beta_B = \frac{\beta_C - \beta_F}{a} + \beta_F + \frac{\beta_C - \beta_F}{2a}\left(k_{ux} - (2 + k_{ut})\right) \tag{34}$$

3.4 Boundary conditions

The simulation of transient flow within pipe systems necessitates a careful interaction between governing equations and boundary conditions. Below is a comprehensive description of how these equations engage with the boundary conditions in the case of a water hammer event triggered by the closure of a downstream valve:

3.4.1 Upstream boundary condition (Reservoir)

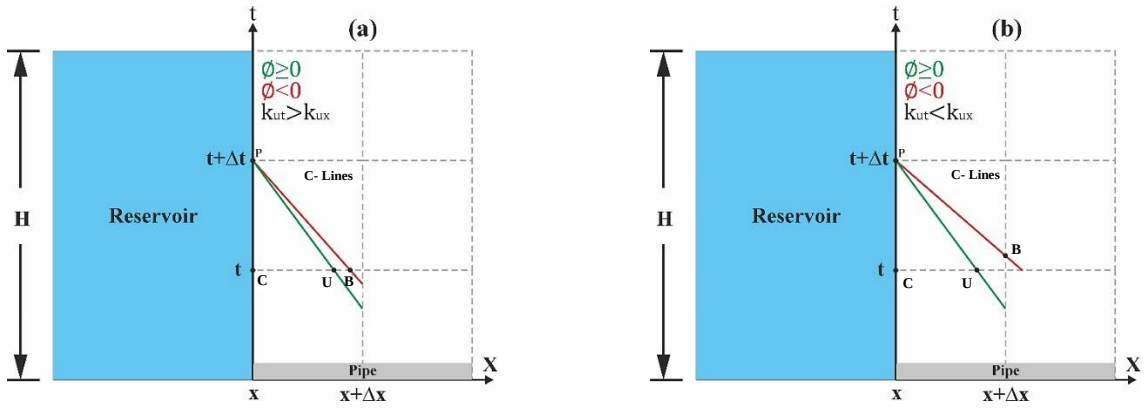

Figure 2 Upstream boundary conditions: (a) when $k_{ut} > k_{ux}$, (b) when $k_{ut} < k_{ux}$.

At the upstream boundary (Figure 2), we typically consider the reservoir's piezometric head (H) to be stable due to its substantial volume compared to the pipe system's flow, that's mean:

$$H = H_c = H_p$$

The C- lines equations are used to compute the discharge (Q) at the upstream boundary nodes, based on the ensuing states:

- $when\ k_{ut} > k_{ux}\ or\ k_{ut} < k_{ux}\ \&\ \emptyset \geq 0$

In order to identify the fluid properties at node P in this state, we will use Equations 16, 14, and 15, respectively.

- $when\ k_{ut} > k_{ux}\ \&\ \emptyset < 0$

While, in this state we will use Equations 22, 20, and 21, respectively.

- $when\ k_{ut} < k_{ux}\ \&\ \emptyset < 0$

In this state we will use Equations 34, 32, and 33, respectively.

3.4.2 Downstream boundary condition (Valve)

At the pipe system's downstream boundary (Figure 3), the valve exerts control over the flow, thereby affecting the discharge (Q) and the piezometric head (H).

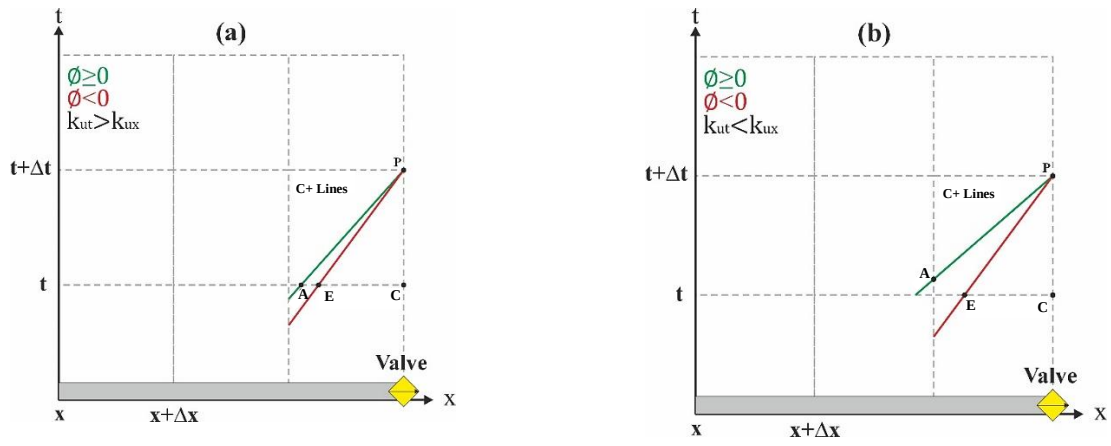

Figure 3 Downstream boundary conditions: (a) when $k_{ut} > k_{ux}$, (b) when $k_{ut} < k_{ux}$

Operation of the valve can be represented by one of the Orifice states, specifically the "Small Orifice" state, which links the discharge (Q) to the valve opening and various fluid characteristics. To determine the fluid properties at the downstream boundary nodes, the governing equations for the C+ lines are utilized in tandem with the Orifice equation, following the steps below:

Taking the ratio of the discharge equation of semi-open orifice to the discharge equation of fully open orifice.

$$\frac{Q_P}{Q_o} = \frac{(c_d\ A)_P\ \sqrt{2gH_P}}{(c_d\ A)_o\ \sqrt{2gH_o}} \tag{35}$$

Where, Q_P represents the discharge at the current valve opening at the time $t + \Delta t$, Q_o stands for the discharge at the fully open valve at the time $t = 0$. The term c_d corresponds to the orifice's discharge coefficient, A_o denotes the area of the fully open orifice (valve), and A_P signifies the area of the orifice (valve) at its current opening.

$$assume\ \tau = \frac{(c_d\ A)_P}{(c_d\ A)_o}$$

Where, τ represents the valve opening ratio parameter. It's determined by comparing the current valve opening to its fully open state, with values varying from 0 (representing a completely closed valve) to 1 (indicating a fully open valve). Following this, Eq 24 will be:

$$Q_P^2 = \frac{Q_o^2\ \tau^2\ H_P}{H_o} \tag{36}$$

- $when\ k_{ut}\ >\ k_{ux}\ \&\ \emptyset \geq 0$

Form Eq.12, head will be:

$$H_P = \frac{(C_+ - Q_P)}{c_a T_{np}} \tag{37}$$

By substitute H_P Equation in Eq.36 we get:

$$Q_P^2 = \frac{Q_o^2\ \tau^2}{H_o}\ \frac{(C_+ - Q_P)}{c_a T_{np}} = \frac{Q_o^2\ \tau^2}{H_o\ c_a}\ \frac{(C_+ - Q_P)}{T_{np}}$$

$$By\ assuming\ c_v = \frac{Q_o^2\ \tau^2}{H_o\ c_a}\ we\ get:$$

$$Q_P^2 = c_v\ \frac{(C_+ - Q_P)}{T_{np}} \rightarrow T_{np} Q_P^2 + c_v Q_P - c_v\ C_+ = 0$$

After neglected the negative root of Q_P we get:

$$Q_P = \frac{1}{2T_{np}}\left(-c_v + \sqrt{c_v^2 + 4T_{np} c_v\ C_+}\right) \tag{38}$$

In order to identify the fluid properties at the downstream boundary nodes, we will use Equations 11, 37, and 38, respectively.

- $when\ k_{ut}\ >\ k_{ux}\ or\ k_{ut} < k_{ux}\ \&\ \emptyset < 0$

Form Eq.30, head will be:

$$H_P = \frac{(C_+ - Q_P)}{c_a T_{pp}} \tag{39}$$

By substitute H_P Equation in Eq.36 and using same previous steps, discharge will be:

$$Q_P = \frac{1}{2T_{pp}}\left(-c_v + \sqrt{c_v^2 + 4T_{pp} c_v\ C_+}\right) \tag{40}$$

In order to identify the fluid properties at the downstream boundary nodes, we will use Equations 29, 39, and 40, respectively.

- $when\ k_{ut} <\ k_{ux}\ \&\ \emptyset \geq 0$

Form Eq.24, head will be:

$$H_P = \frac{(C_+ - Q_P)}{c_a T_{np}} \tag{41}$$

By substitute H_P Equation in Eq.36 and using same previous steps, discharge will be:

$$Q_P = \frac{1}{2T_{np}}\left(-c_v + \sqrt{c_v^2 + 4T_{np}c_v\, C_+}\right) \tag{42}$$

In order to identify the fluid properties at the downstream boundary nodes, we will use Equations 23, 41, and 42, respectively.

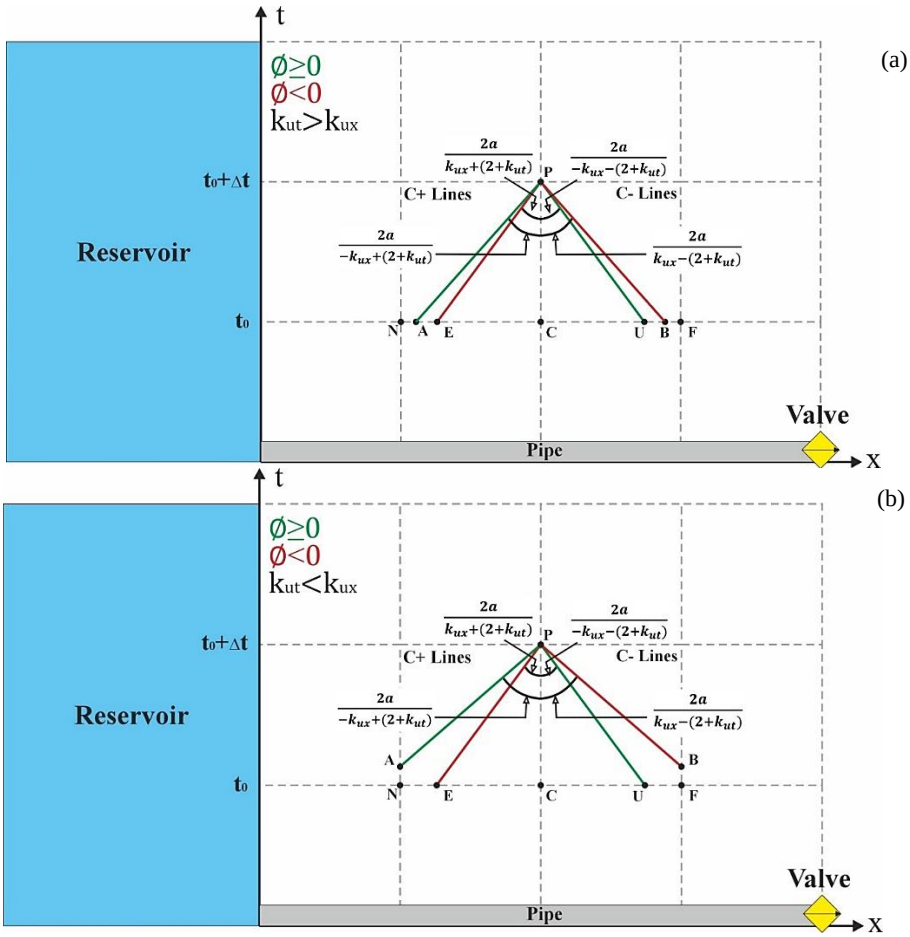

Figure 4 Interior nodes boundary conditions: $(a)\ when\ k_{ut} > k_{ux}, (b)\ when\ k_{ut} < k_{ux}$.

3.4.3 Interior nodes

At the interior nodes (Figure 4), there will be an intersection between the C+ and C- characteristic lines. To determine the fluid properties at these nodes, we need to solve the governing equations for these lines simultaneously, while taking into account any alterations in pipe geometry or fluid properties. The solution derived provides the updated discharge (Q) and piezometric head (H) values at the interior nodes for the subsequent time step. To identify the fluid properties at the interior boundary nodes, we have eight distinct cases which are:

- Case 1: When $k_{ut} > k_{ux}$ & $\emptyset \geq 0$ at C+ & C- lines.

By adding Eq.12 to Eq.15, we will get the following equation.

$$Q_P = \frac{C_+ T_{nn} - C_- T_{np}}{T_{nn} - T_{np}} \tag{43}$$

In addition, by using Eq.12, Eq.13, Eq.11, Eq.16 and Eq.14, we will find the value of H_P, β_A, C_+, β_U and C_- respectively.

- Case 2: When $k_{ut} > k_{ux}$ & $\emptyset \geq 0$ at C+ lines & $\emptyset < 0$ at C- lines.

By adding Eq.12 to Eq.21, we will get the following equation.

$$Q_P = \frac{C_+ T_{pn} - C_- T_{np}}{T_{pn} - T_{np}} \tag{44}$$

In addition, by using Eq.12, Eq.13, Eq.11, Eq.22 and Eq.20, we will find the value of H_P, β_A, C_+, β_B and C_- respectively.

- Case 3: When $k_{ut} > k_{ux}$ & $\emptyset < 0$ at C+ & C- lines.

By adding Eq.18 to Eq.21, we will get the following equation.

$$Q_P = \frac{C_+T_{pn} - C_-T_{pp}}{T_{pn} - T_{pp}} \tag{45}$$

In addition, by using Eq. 18, Eq.19, Eq. 17, Eq.22 and Eq.20, we will find the value of H_P, β_E, C_+, β_B and C_- respectively.

- Case 4: When $k_{ut} > k_{ux}$ & $\emptyset < 0$ at C+ lines & $\emptyset \geq 0$ at C- lines.

By adding Eq.15 to Eq.21, we will get the following equation.

$$Q_P = \frac{C_+T_{nn} - C_-T_{pp}}{T_{nn} - T_{pp}} \tag{46}$$

In addition, by using Eq. 18, Eq.19, Eq. 17, Eq.16 and Eq.14, we will find the value of H_P, β_E, C_+, β_U and C_- respectively.

- Case 5: When $k_{ut} < k_{ux}$ & $\emptyset \geq 0$ at C+ & C- lines.

By adding Eq.24 to Eq.27, we will get the following equation.

$$Q_P = \frac{C_+T_{nn} - C_-T_{np}}{T_{nn} - T_{np}} \tag{47}$$

In addition, by using Eq.24, Eq.25, Eq.23, Eq.28 and Eq.26, we will find the value of H_P, β_A, C_+, β_U and C_- respectively.

- Case 6: When $k_{ut} < k_{ux}$ & $\emptyset \geq 0$ at C+ lines & $\emptyset < 0$ at C- lines.

By adding Eq. 24 to Eq.33, we will get the following equation.

$$Q_P = \frac{C_+T_{pn} - C_-T_{np}}{T_{pn} - T_{np}} \tag{48}$$

In addition, by using Eq.24, Eq.25, Eq.23, Eq.34 and Eq.32, we will find the value of H_P, β_A, C_+, β_B and C_- respectively.

- Case 7: When $k_{ut} < k_{ux}$ & $\emptyset < 0$ at C+ & C- lines.

By adding Eq.30 to Eq. 33, we will get the following equation.

$$Q_P = \frac{C_+T_{pn} - C_-T_{pp}}{T_{pn} - T_{pp}} \tag{49}$$

In addition, by using Eq. 30, Eq.31, Eq.29, Eq. 34 and Eq.32, we will find the value of H_P, β_E, C_+, β_B and C_- respectively.

- Case 8: When $k_{ut} < k_{ux}$ & $\emptyset < 0$ at C+ lines & $\emptyset \geq 0$ at C- lines.

By adding Eq. 30 to Eq.27, we will get the following equation.

$$Q_P = \frac{C_+T_{nn} - C_-T_{pp}}{T_{nn} - T_{pp}} \tag{50}$$

In addition, by using Eq. 30, Eq.31, Eq.29, Eq.28 and Eq.26 we will find the value of H_P, β_E, C_+, β_U and C_- respectively.

3.5 Experimental data

The empirical basis of this study was drawn from two distinct sources of experimental data: firstly, from the Hydraulic Laboratory of the University of South Carolina (USC), derived from a prior research study conducted by [12], and secondly, from a research paper conducted by [25]. The experimental setup at USC included a pressure reservoir positioned upstream, a copper pipe extending 158.71 meters long and 25.4 millimeters in diameter, and a downstream valve. The data extracted from this setup included pressure sensor readings from a location near the valve. While, [25] data involved a long copper pipe of 98.11 m in length and 16 mm in diameter, along with a downstream ball valve with a closure time not exceeding 0.003 milliseconds. In this instance, the collected data included pressure sensor readings taken from several pipe points. A sudden valve closure was initiated in both experimental scenarios to generate the transient conditions. To establish a wide range of experimental conditions, the researchers conducted a series of tests to explore the behaviors of transient flows in pipe systems under various operational circumstances, such as different water reservoir fill levels and varied flow velocities. The experimental data compiled from both setups encompasses measurements of various fluid properties like pressure head over time, initial flow rate, and other pertinent parameters during the transient flow events. Table 2 summarizes each experiment's principal parameters, including initial water levels, flow velocities, and friction coefficients. In this study, the wave speed was calculated based on experimental data, relying on extracting the average wave speeds for each cycle during a set of different cycles, as shown in the following equation $a_{avg} = 1/n \sum_{i=1}^{n}(2L/t_i)$. The commonly used trial and error methods were utilized to determine the damping coefficients (k, k_{ut}, k_{ux}) values (12,22).

Table 2 System data for experiments tests used for model validation and verification

Test No.	v_0 (m/s)	H (m)	Re	a_{avg} (m/s)	k trial& error	k_{ux} trial& error	k_{ut}	Sensor Location at Pipe
1	0.309	34.36	7845	1203.5	0.035	0.035	0	Valve
2	0.255	33.59	6482	1217.1	0.032	0.032	0	Valve
3	0.31	30.34	7876	1217.5	0.031	0.031	0	Valve
4	0.213	21.10	5419	1180.4	0.045	0.045	0	Valve
5	0.171	16.08	4348	1150.5	0.051	0.051	0	Valve
6	0.94	127.42	15843	1298.4	0.01	0.01	0	Valve, middle & 75% L

*Experimental data for tests 1-5 were extracted from [12], whereas test 6 was obtained from [25].

The range of scenarios provided by these experiments serves as a robust platform to evaluate the effectiveness of our numerical models for transient flow, utilizing both Steady and Unsteady Friction Models via the Characteristics Method. In the subsequent sections, we'll exhibit the outcomes of our numerical simulations and contrast them against the experimental data. This will enable us to assess the precision and dependability of our models under varying operational conditions.

4. Results and discussions

4.1 Comparison of steady and 1-k IAB friction models

This section focuses on validating numerical models by comparing the results derived from the steady friction and the 1-k IAB models with the experimental data. This comparison aims to highlight the strengths and weaknesses of each model in simulating water hammer events. The results demonstrated in Figure 5 indicate that the steady friction model accurately identifies the first two peaks of the water hammer event in relation to all experimental data [26], which is attributed to the water hammer's insensitivity to dissipation at its onset [12]. However, the model's precision diminishes when estimating the amount of damping that occurs during the propagation of the water hammer. This can be attributed to the model only accounting for losses from wall friction when calculating energy losses [12], neglecting additional dynamic changes in fluid flow.

Conversely, the 1-k IAB model's results reasonably depict damping and provide a more holistic and accurate representation of the water hammer event throughout its duration. This model's ability to accurately capture the true damping behavior of pressure waves is attributed to the inclusion of unsteady friction terms in the governing equations, which account for the losses resulting from dynamic changes in fluid flow properties during the water hammer. Such changes are triggered by swift shifts in transient pressures and flow rates that induce increased turbulent shear stresses between the layers of flowing liquid [3], and the fluid's resistance to these changes [12]. During pressure wave propagation in the IAB model, some cases exhibit a temporal mismatch in pressure wave timing compared to the experimental data. This discrepancy tends to amplify over time, decreasing the model's accuracy by simulating the frequency and speed of water hammer waves. As a result, this temporal discrepancy emerges as a significant drawback of the 1-k IAB model [22].

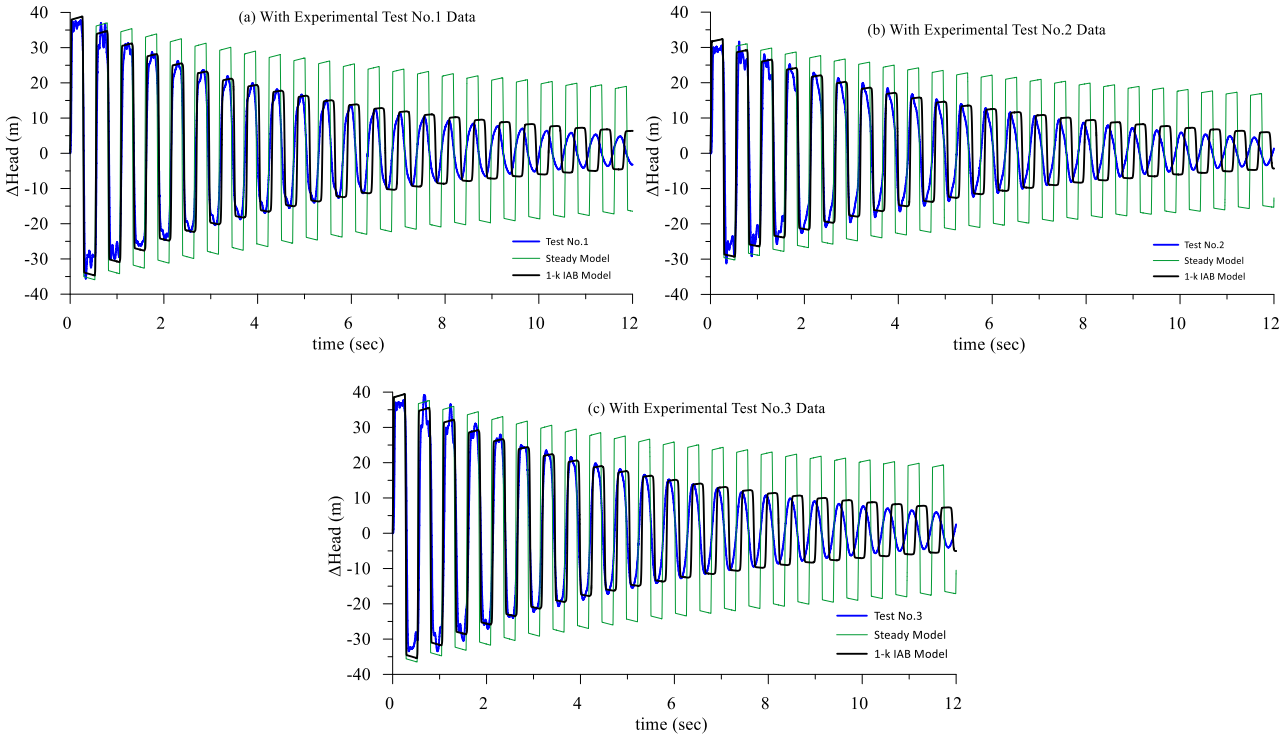

Figure 5 Comparison between the experimental data and steady and 1-k IAB friction models at valve location downstream of the pipeline.

4.2 Comparison of 1-k IAB and 2-k IAB friction models

As with the 1-k IAB model, the 2-k IAB unsteady friction model demonstrated its ability to accurately represent the amount of damping during the event period, as it could accurately monitor the true damping behavior of the pressure wave peaks. In this comparison, nearly identical damping results were observed for both friction models (Figure 6). This is attributed to using the same values for the damping coefficient k and the convective acceleration coefficient k_{ux}, as the convective acceleration term is responsible for describing the actual damping of the water hammer. In contrast, better accuracy was noted in simulating the shift of pressure wave peaks in the 2-k IAB model compared to the 1-k IAB model. This is due to the separation of the convective and local acceleration terms in the 2-k IAB model into two separate coefficients, which allowed the damping coefficient to be separated from the coefficient responsible for wave speed correction, thereby giving more freedom in capturing the dynamic changes in fluid flow characteristics by capturing the damping amount of the wave and its speed without affecting one another. In this comparison, through the trial-and-error method, we found that setting $k_{ut} = 0$ yielded optimal results. This finding can be attributed to the fact that the local acceleration coefficient k_{ut} is responsible for correcting the wave speed in the simulation [15]. This means that using the correct wave speed for the experiment as an average wave speed may lead to better results when replacing the value of k_{ut} with zero.

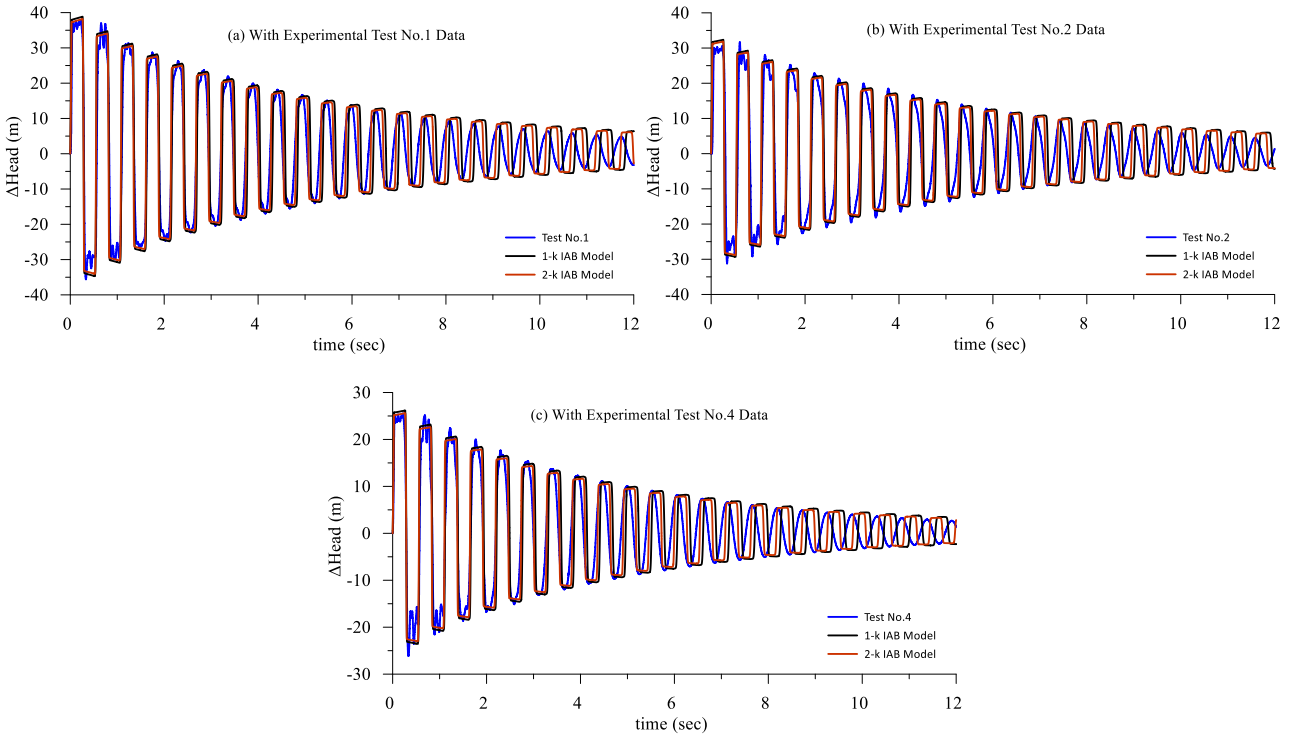

Figure 6 Comparison between the experimental data and 1-k IAB and 2-k IAB friction models at valve location downstream of the pipeline

It is worth to mention here that the time lag observed in the runs for damping wave after time 6 sec primarily arises from numerical approximations associated with using the Method of Characteristics (MOC) and the selection of friction models. Specifically, in the 1-k IAB model, the convective acceleration term is responsible for capturing the damping effect, but it does not fully account for the correction of wave speed, that may lead to discrepancies in pressure wave arrival times.

To ensure the reliability and accuracy of the 2-k IAB model, the model was tested at different points in the pipe, and its results were compared with the experimental data, as shown in Figure 7. The results obtained were consistent with what was previously proposed, where we notice that the model effectively captures the damping of pressure waves and their propagation, very closely approximating the experimental data. In addition to capturing the shift in pressure waves and their speed, this accurately shows the water hammer phenomenon throughout the event's duration.

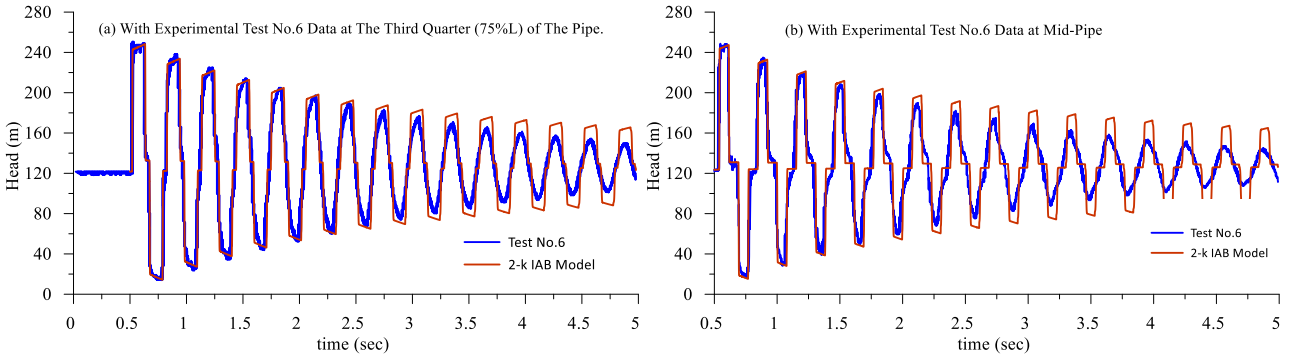

Figure 7 Comparison between the experimental data and the results of the 2-k IAB friction model at different points of the pipe

4.3 Statistical analysis for results of friction models

After providing a visual comparison of the friction models through the previous figures, the following table offers a detailed statistical evaluation of these models. Table 3 provides a clear comparison between the friction models analytically using the NRMSE method as a statistical measure. This method allows for an accurate quantitative evaluation of the models, drawing attention to the subtle differences in their performance that may not immediately appear in graphical representations. Therefore, it provides a deeper understanding of the accuracy of friction models in simulating the water hammer phenomenon.

Table 3 System data for experimental tests used to validate the models

Test No.	NRMSE		
	Steady Model	**1-k IAB Model**	**2-k IAB Model**
1	0.2005	0.1283	0.0894
2	0.2082	0.1273	0.0968
3	0.1991	0.1163	0.0934
4	0.2213	0.1129	0.0806
5	0.2292	0.0977	0.0686
6	0.1234	0.1175	0.1082

As shown in the table above, the statistical analysis results are consistent with the visual comparisons of the friction models, confirming that the 2-k IAB unsteady friction model showed superior performance by providing more accurate and reliable results compared to the other friction models. The 1-k IAB follows the 2-k IAB, while the steady friction model is the least accurate.

4.4 Discussion of 2-k IAB models

This model was developed as an improved version of the 1-k IAB model to get rid of its inherent limitations. Improvement was achieved by separating the effect of local acceleration from convective acceleration by using a different coefficient for each acceleration. This strategy led to a more accurate and flexible model than the previous one, especially in cases where $k_{ut} \geq k_{ux}$. However, it's essential to point out that this model might exhibit instability in the system or lead to illogical results in situations where $k_{ut} < k_{ux}$ (12), as is demonstrated in the cases below:

- Obtaining unreasonable results in terms of wave displacement when $k_{ut} < k_{ux}$, as shown in Figure 8, where the effect of k_{ut} on wave displacement was observed to be weaker than in cases of $k_{ut} \geq k_{ux}$, even though the change magnitude is the same ±0.002.

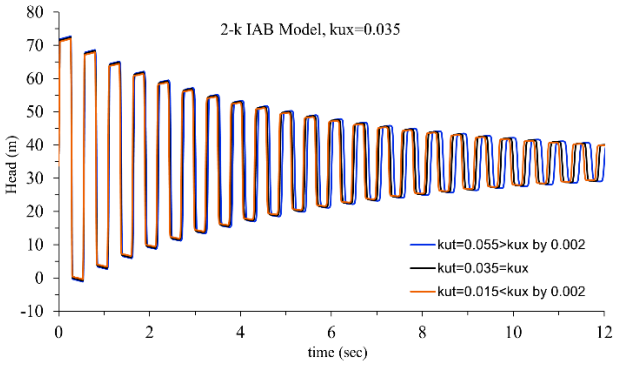

Figure 8 Illogical results in the 2-k IAB model when using k_{ut} values lower than k_{ux}

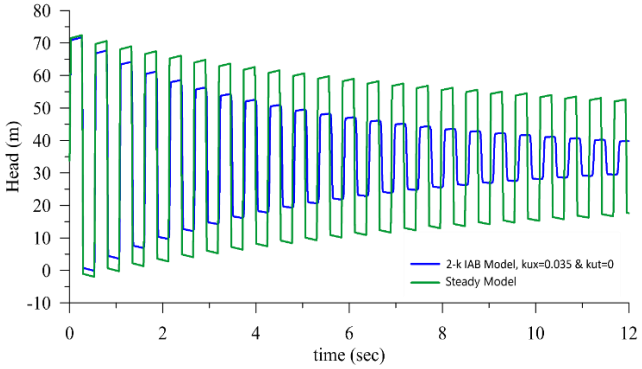

Figure 9 The illogical outcomes of the 2-k IAB model when setting the value of k_{ut} to zero, compared with the steady friction model.

- The results are illogical when substituting $k_{ut} = 0$.

$$\frac{\partial H}{\partial x} + \frac{1}{g}\frac{\partial v}{\partial t} + \frac{1}{g}\left(k_{ut}\frac{\partial v}{\partial t} + k_{ux}\emptyset * a\frac{\partial v}{\partial x}\right) + \frac{f}{D} * \frac{v^2}{2g} = 0 \ldots\ldots\ldots \text{Momentum Equation}$$

In the Momentum Equation, since the term $(k_{ux}\ \emptyset * a\ \partial v/\partial x)$ is the factor affecting the amount of pressure wave damping, while the term $(k_{ut}\ \partial v/\partial t)$ is the factor influencing the amount of pressure wave displacement. This means that when $k_{ut} = 0$ in this model, the amount of pressure wave displacement should be equal to the displacement in the steady friction model. What was observed, however, was a clear difference between the two friction models in the intermediate and final stages of the simulation, despite assuming $k_{ut} = 0$ in the 2-k IAB model, as clearly shown in Figure 9.

5. Conclusion

This research paper aimed to develop and validate numerical models for simulating transient flow in pipe systems using steady and unsteady friction models based on the MOC. The study focused on analyzing and comparing the performance of different friction models in predicting transient events resulting from valve closure. The results showed that the steady friction model effectively captured the first pressure peaks of the water hammer event in most cases. However, it demonstrated limitations in accurately describing the damping and propagation of subsequent pressure peaks. On the other hand, the unsteady friction model 1-k IAB model provided a

more accurate representation of the damping and a comprehensive depiction of water hammer events throughout the duration of transient flow. Still, it showed a time discrepancy in the timing of pressure waves and their shift compared to experimental data. This discrepancy tends to increase over time, leading to decreased accuracy in simulating the frequency and speed of water hammer waves. The 2-k IAB model presented a similar representation to the 1-k IAB model in simulating the damping of pressure wave peaks throughout the transient event. However, it demonstrated less temporal discrepancy in the timing of pressure waves and their shift compared to experimental data. This led to higher simulation accuracy compared to previous models. However, this increase in accuracy compared to the 1-k IAB model is insufficient to justify the use of this model, given the additional complexities and high computational costs when applying it. This might be attributed to the model's instability and the illogical results produced for $k_{ut} < k_{ux}$, as previously mentioned. This might explain why researchers rarely use this model. The developed unsteady friction model also captures water hammer events at different locations in the pipe. This also demonstrates the versatility of this model and its applicability in capturing transient flow events across different pipe systems. In conclusion, this research paper highlights the importance of selecting the appropriate friction models for simulating transient events in pipe systems. The unsteady friction models provide a more reliable and accurate representation of water hammer events than the steady friction model, especially in scenarios where secondary pressure peaks need to be considered. In the case of unsteady friction models, the 2-k IAB model is better at capturing pressure wave peaks and their time variations than the 1-k IAB model. Further research can focus on developing and improving the 2-k IAB model to address the errors and illogical results encountered when $k_{ut} < k_{ux}$, to obtain more accurate and reliable results than the current model. Future studies can contribute to a more comprehensive understanding of transient flow events and their impact on pipe systems.

6. References

[1] Urbanowicz K, Bergant A, Stosiak M, Towarnicki K. Analytical solutions of water hammer in metal pipes. Part II—Comparative study. In: Lesiuk G, Duda S, Correia JAFO, De Jesus AMP, editors. Fatigue and Fracture of Materials and Structures. Structural Integrity, vol 24. Cham: Springer; 2022. p. 69-83.

[2] Henclik S. Analytical solution and numerical study on water hammer in a pipeline closed with an elastically attached valve. J Sound Vib. 2018;417:245-59.

[3] EL-Turki A. Modeling of hydraulic transients in closed conduits [thesis]. Fort Collins: Colorado State University; 2013.

[4] Urbanowicz K, Bergant A, Stosiak M, Karpenko M, Bogdevičius M. Developments in analytical wall shear stress modelling for water hammer phenomena. J Sound Vib. 2023;562:117848.

[5] Urbanowicz K, Jing H, Bergant A, Stosiak M, Lubecki M. Progress in analytical modeling of water hammer. J Fluids Eng. 2023;145(8):081203.

[6] Joukowsky N. Über den hydraulischen Stoss in Wasserleitungsrohren. Saint Petersburg: The Imperial Academy of Science; 1900. (In German)

[7] Ghidaoui MS, Zhao M, McInnis DA, Axworthy DH. A review of water hammer theory and practice. Appl Mech Rev. 2005;58(1):49-76.

[8] Abdeldayem OM, Ferràs D, van der Zwan S, Kennedy M. Analysis of unsteady friction models used in engineering software for water hammer analysis: Implementation case in Wanda. Water. 2021;13(4):495.

[9] Chaudhry MH. Applied hydraulic transients. 3rd ed. New York: Springer; 2014.

[10] Bhattacharyya EM, Saikia MD, Das MM. Development of numerical model for transients in pipe flow for water hammer situation and comparison of different friction equations for transient friction. Int Res J Eng Technol. 2018;5(3):2995-3001.

[11] Yu C, Yu X, Zhang L, Neupane B, Zhang J. Approximate approach for improving pressure attenuation accuracy during hydraulic transients. Water Supply. 2022;22(3):3387-98.

[12] Khilqa S, Elkholy M, Al-Tofan M, Caicedo JM, Chaudhry MH. Damping in transient pressurized flows. J Hydraul Eng. 2019;145(10):04019034.

[13] Kjerrumgaard Jensen R, Kær Larsen J, Lindgren Lassen K, Mandø M, Andreasen A. Implementation and validation of a free open source 1d water hammer code. Fluids. 2018;3(3):64.

[14] Prashanth Reddy H, Silva-Araya WF, Hanif Chaudhry M. Estimation of decay coefficients for unsteady friction for instantaneous, acceleration-based models. J Hydraul Eng. 2012;138(3):260-71.

[15] Storli PT, Nielsen TK. Transient friction in pressurized pipes. II: two-coefficient instantaneous acceleration–based model. J Hydraul Eng. 2011;137(6):679-95.

[16] Urbanowicz K, Bergant A, Stosiak M, Deptuła A, Karpenko M, Kubrak M, et al. Water hammer simulation using simplified convolution-based unsteady friction model. Water. 2022;14(19):3151.

[17] Shamloo H, Norooz R, Mousavifard M. A review of one-dimensional unsteady friction models for transient pipe flow. Cumhuriyet Science Journal. 2015;36(3):2278-88.

[18] al-Yassiri HM, Ali KH, Jalil JM. Three-dimensional numerical study of flow characteristics through a centrifugal pump. Al-Rafidain Eng J. 2008;16(1):75-88.

[19] Zhang B, Wan W, Shi M. Experimental and numerical simulation of water hammer in gravitational pipe flow with continuous air entrainment. Water. 2018;10(7):928.

[20] Arefi MH, Ghaeini-Hessaroeyeh M, Memarzadeh R. Numerical modeling of water hammer in long water transmission pipeline. Appl Water Sci. 2021;11(8):140.

[21] Duan X, Zhu J, Li X, Tang X. Comprehensive application analyses of elastic models and viscoelastic models in transient flows in polymeric pipelines. J Hydroinformatics. 2022;24(5):1020-52.

[22] Cao Z, Wang Z, Deng J, Guo X, Lu L. Unsteady friction model modified with compression-expansion effects in transient pipe flow. Aqua Water Infrastruct Ecosyst Soc. 2022;71(2):330-44.

[23] Jensen RK, Larsen JK, Lassen KL. Modelling of a two phase water hammer [thesis]. Esbjerg: Aalborg University Esbjerg; 2018.

[24] Pal S, Hanmaiahgari PR, Karney BW. An overview of the numerical approaches to water hammer modelling: the ongoing quest for practical and accurate numerical approaches. Water. 2021;13(11):1597.

[25] Adamkowski A, Lewandowski M. Experimental examination of unsteady friction models for transient pipe flow simulation. J Fluids Eng. 2006;128(6):1351-63.

[26] Mohsin ZZ, Sulaiman ZA. Application of the method of characteristics with unsteady friction model for numerical modeling of transient flow induced by valve closure. Al-Rafidain Eng J. 2023;28(2):209-25.